JOURNAL OF THERMOPHYSICS AND HEAT TRANSFER
Vol. 11, No. 4, October–December 1997

Discrete Ordinates Algorithm for Domains with Embedded Boundaries

Louis H. Howell* and Vincent E. Beckner†
Lawrence Berkeley Laboratory, University of California, Berkeley, Berkeley, California 94720

Embedded boundary methods model fluid flows in complex geometries by treating boundaries as tracked interfaces in a regular mesh. Though often referred to as Cartesian grid methods, they are equally well-suited to axisymmetric problems. This paper describes a formulation of the discrete ordinates method for radiative transfer calculations with embedded boundaries. The method uses diamond-difference stencils in the interior with a conservative extension to boundary cells based on a volume-of-fluid approach. Numerical examples are presented in both two-dimensional Cartesian and axisymmetric geometries, including a model of the BERL 300-kW natural gas burner.

Nomenclature

F	=	volume fraction, $\in[0, 1]$
f	=	area fraction, $\in[0, 1]$
I_b	=	blackbody intensity, $\sigma_b T^4/\pi$, W/(m^2 sr)
$I_{p,q}$, I_m	=	radiant intensity, W/(m^2 sr)
L^w	=	length of embedded boundary segment, m
m	=	ordinate index, Cartesian coordinates
$\hat{n}$	=	unit normal to embedded boundary segment
p, q	=	ordinate indices, axisymmetric coordinates
S	=	source term, W/(m^3 sr)
w	=	superscript for quantities at the wall
$w_{p,q}$, w_m	=	ordinate weight
α	=	dimensionless parameter in angular difference
ε, ρ	=	wall emissivity and reflectivity
κ, σ	=	absorption and scattering coefficients, m^{-1}
μ, ξ, η	=	direction cosines
$\Omega_{p,q}$, Ω_m	=	ordinate direction unit vector
$\lceil x \rceil$	=	max(x, 0)
$\lfloor x \rfloor$	=	min(x, 0)

Introduction

EMBEDDED boundary methods have proven to be a robust and competitive approach to computing fluid flows in complex geometries. First introduced by Purvis and Burkhalter,[1] they have been used successfully both in compressible calculations with adaptive mesh refinement[2,3] and, more recently, in incompressible calculations as well.[4] Reference 5 presented some results using this approach to model combustion in a gas-fired burner, with the radiative transfer effects discretized using a discrete ordinate method. Our intent in this paper is to give a more complete and validated presentation of the discrete ordinate method with embedded boundaries, which was only briefly introduced in Ref. 5.

The basic idea behind embedded boundaries is to use a regular mesh to cover the computational domain, then block off those parts of the grid that are inside the chamber walls or any solid obstructions. Previous work of this nature with the discrete ordinate method has been presented by Chai et al.[6] In their approach computational cells are marked as being either fluid cells or body cells, i.e., interior or exterior, respectively, giving the embedded boundary a stairstep appearance. In contrast, our present work treats the boundary more as a piecewise-linear tracked front, and so a third kind of cell, the mixed cell, has been added to the model. This approach is consistent with that taken in Ref. 3, permitting us to use the same data structures for fluid dynamics and radiation and to compute coupled solutions such as the ones in Ref. 5.

We will begin by briefly presenting the discrete ordinate discretization for an axisymmetric coordinate system. This is not new work, but will serve to introduce the notation and provide a framework for introducing the embedded boundary. The discretization for Cartesian coordinates is a limiting case of the axisymmetric discretization, and does not need to be presented separately. Next, we will develop stencils for representing the embedded boundary in Cartesian coordinates, and then extend these stencils to cover the axisymmetric case. Finally, we will present validation results and some numerical examples.

Method with Flat Walls

The discrete ordinates representation of the radiative transport equation with isotropic scattering in axisymmetric coordinates, discretized as a conservation relation for each cell, is

$$\frac{\mu_{p,q}}{r_i \Delta r}\left(r_{i+1/2} I_{p,q,i+1/2,j} - r_{i-1/2} I_{p,q,i-1/2,j}\right) + \frac{\xi_p}{\Delta z}\left(I_{p,q,i,j+1/2} - I_{p,q,i,j-1/2}\right) + \frac{1}{r_i w_{p,q}}\left(\alpha_{p,q+1/2} I_{p,q+1/2,i,j} - \alpha_{p,q-1/2} I_{p,q-1/2,i,j}\right) + (\kappa + \sigma) I_{p,q,i,j} = \kappa I_{b,i,j} + \frac{\sigma}{4\pi} \sum_{p',q'} w_{p',q'} I_{p',q',i,j} \tag{1}$$

where quantities with half-indices exist at cell faces. The subscript p identifies a level of ordinate directions with a particular value of ξ, while q indexes the separate ordinates sharing that level; the ordinate weights $w_{p,q}$ are normalized so that $\Sigma_{p,q} w_{p,q} = 4\pi$. The right-hand side of Eq. (1), representing the emission and scattering sources, will hereafter be abbreviated as S. The angular differencing parameters α are related to the direction cosines and weights by the relation $\alpha_{p,q+1/2} - \alpha_{p,q-1/2} = -w_{p,q}\mu_{p,q}$. The Cartesian coordinates form of Eq. (1) can be obtained by removing the angular differencing term and the references to r.

Detailed derivations of these equations can be found in Refs. 7 and 8, as can most aspects of the solution procedure. To

Received Oct. 7, 1996; revision received Feb. 24, 1997; accepted for publication April 21, 1997.

*Mathematician, Center for Computational Sciences and Engineering.

†Computer Systems Engineer, Center for Computational Sciences and Engineering.

summarize briefly, we relate the face- and cell-based quantities in Eq. (1) using diamond-difference formulas

$$I_{p,q,i-1/2,j} + I_{p,q,i+1/2,j} = I_{p,q,i,j-1/2} + I_{p,q,i,j+1/2} = I_{p,q-1/2,i,j} + I_{p,q+1/2,i,j} = 2I_{p,q,i,j} \tag{2}$$

For each ordinate direction, we sweep through the mesh in the direction of propagation. When μ and ξ are positive, this involves solving for $I_{p,q,i,j}$, $I_{p,q,i+1/2,j}$, $I_{p,q,i,j+1/2}$, and $I_{p,q+1/2,i,j}$ in terms of $I_{p,q,i-1/2,j}$, $I_{p,q,i,j-1/2}$, and $I_{p,q-1/2,i,j}$. In some cases, one of the computed edge quantities can be negative. Since negative fluxes are nonphysical and can lead to spurious oscillations, we set the offending quantities to zero and recompute the other dependent fluxes. The ability to perform this flux limiting in a relatively straightforward manner is the main motivation for choosing the cell- and face-based diamond difference formulation over the otherwise equivalent node-based bilinear formulation.

To incorporate the flux limiting operation into a vector loop, we observe that the cell-centered flux $I_{p,q,i,j}$ takes on its smallest possible value when the correct combination of dependent face fluxes is limited. The sign of one flux may depend on which others are limited, and so it is necessary to consider all eight combinations separately. The additional computation is not excessive, however, since many terms common to all flux combinations may be precomputed. The general form for the central flux computation is

$$I_{p,q,i,j} = \left[S_{i,j} + \frac{\mu_{p,q}}{r_i \Delta r}(l_\mu r_{i+1/2} + r_{i-1/2}) I_{p,q,i-1/2,j} + \frac{\xi_p}{\Delta z}(l_\xi + 1) I_{p,q,i,j-1/2} + \frac{1}{r_i w_{p,q}}(l_\alpha \alpha_{p,q+1/2} + \alpha_{p,q-1/2}) I_{p,q-1/2,i,j} \right] \Bigg/ \left(\kappa + \sigma + l_\mu \frac{2\mu_{p,q} r_{i+1/2}}{r_i \Delta r} + l_\xi \frac{2\xi_p}{\Delta z} + l_\alpha \frac{2\alpha_{p,q+1/2}}{r_i w_{p,q}} \right) \tag{3}$$

where l_μ, l_ξ, and l_α are each 0 or 1, depending on whether the corresponding face is or is not limited, respectively. Once $I_{p,q,i,j}$ has been determined as the minimum of its eight possible values, we set

$$I_{p,q,i+1/2,j} = \max(2I_{p,q,i,j} - I_{p,q,i-1/2,j}, 0) \tag{4}$$

and likewise with $I_{p,q,i,j+1/2}$ and $I_{p,q+1/2,i,j}$.

The computation begins at the outer boundary with inward-directed ordinates and proceeds through increasing values of $\mu_{p,q}$ for each ξ_p. Zero-weight starting directions, satisfying the Cartesian coordinates form of Eq. (1), are used to obtain each $I_{p,1/2}$.

Reflecting wall boundaries and the scattering source can be accounted for by iteration in the manner of Ref. 9. Since our primary focus in this paper is the treatment of wall boundaries, we will not concern ourselves with the details of the scattering solution. The equation to be satisfied at the outer (r) wall of the domain is

$$I_{p,q} = \varepsilon I_b^w + \frac{\rho}{\pi} \sum_{\mu_{p',q'}>0} w_{p',q'} \mu_{p',q'} I_{p',q'}, \qquad \mu_{p,q} < 0 \tag{5}$$

and similarly for the top and bottom (z) walls. This equation implicitly assumes that the ordinate set has a half-range first moment exactly equal to π. Ordinate sets with this property, for walls aligned with the coordinate axes, are given in Refs. 10 and 11. At the $r = 0$ boundary we follow the suggestion of Ref. 8 and set each outward $I_{p,q}$ to the w-weighted average of the inward fluxes on the same p level.

It is not necessary to store interior fluxes for all ordinate directions at once, but it is convenient to store fluxes for each ordinate along edges where the radiation meets a wall. This permits us to update the reflection sources after each ordinate sweep, so that all of the source information is up-to-date before starting the sweep for the next ordinate direction.

Discretization at an Embedded Boundary

Many calculations involve more complicated geometries, which we model as embedded boundaries. (This is often called the Cartesian grid method, even though it works just as well for axisymmetric coordinates.) Geometry information is represented on the entire grid as volume fractions for each cell and area fractions for each face. These fractions are 1 for fluid cells, and 0 for body cells, with intermediate values in the partial cells at the boundary.

To adapt the radiation solver to this algorithm framework, we derived a form of the discrete ordinate discretization that is valid for all three cell types and reduces to the usual form given in the preceding text for cells entirely in the fluid. The advantages of this approach are that separate coding for boundary cells is minimized, boundary cells are updated in the same vector loop as interior cells, and they are updated in the proper order following the radiation flow so that information lags do not degrade the convergence rate.

Cartesian Coordinates

It is easiest to start the derivation with a true Cartesian coordinate system, and because this formulation applies to the zero-weight starting directions for axisymmetric coordinates, the formulas will be useful for both geometries. The conservation relation in each cell becomes

$$\frac{\mu_m}{\Delta x}(f_{i+1/2,j} I_{m,i+1/2,j} - f_{i-1/2,j} I_{m,i-1/2,j}) + \frac{\xi_m}{\Delta y}(f_{i,j+1/2} I_{m,i,j+1/2} - f_{i,j-1/2} I_{m,i,j-1/2}) + \frac{\hat{n}\cdot\boldsymbol{\Omega}_m}{\Delta x \Delta y} L_{i,j}^w I_{m,i,j}^w + (\kappa + \sigma) F_{i,j} I_{m,i,j} = F_{i,j} S_{i,j} \tag{6}$$

where $I_{m,i,j}^w$ is the intensity at the wall. (We use a single subscript m to denote the ordinate direction in Cartesian coordinates, because there is no angular coupling and, hence, no need to distinguish the sets of ordinates sharing a value of ξ.) $L_{i,j}^w$ is the length of the embedded boundary segment (if any) in the cell. The quantity $(\hat{n}\cdot\boldsymbol{\Omega}_m)$ is the component of ordinate $\boldsymbol{\Omega}_m$ along the unit normal $\hat{n}$ of the boundary segment, and so the flux across that segment is $(\hat{n}\cdot\boldsymbol{\Omega}_m) L_{i,j}^w I_{m,i,j}^w$. Figure 1 may make the flux balance in the cell more clear. The contribution from flux across the embedded boundary appears to require values

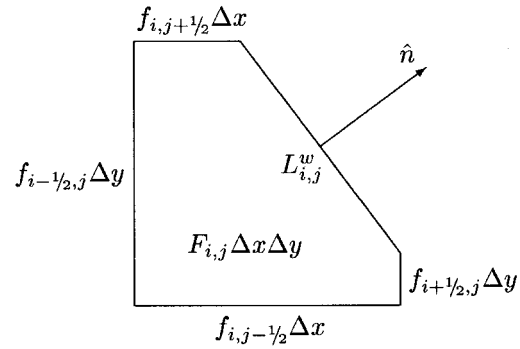

Fig. 1 Cell containing a segment of the embedded boundary.

for $\hat{n}$ and L^w for each cell, but this term can be rewritten in terms of volume and area fractions by considering a uniform flow in empty space:

$$\frac{\mu_m}{\Delta x}(f_{i+1/2,j} - f_{i-1/2,j}) + \frac{\xi_m}{\Delta y}(f_{i,j+1/2} - f_{i,j-1/2}) + \frac{\hat{n}\cdot\Omega_m}{\Delta x\Delta y}L^w_{i,j} = 0 \tag{7}$$

The diamond difference formulation is based on taking a multilinear profile across each cell to express $I_{m,i+1/2,j}$ in terms of $I_{m,i-1/2,j}$ and $I_{m,i,j}$, and similarly for $I_{m,i,j+1/2}$. With embedded boundaries we must consider the possibility that $I_{m,i-1/2,j}$ may not be available, if that face of the cell is entirely outside the fluid region. Permitting the discretization to drop to first order at the boundary, we modify the diamond difference formulas as follows:

$$I_{m,i+1/2,j} = I_{m,i,j} + f_{i-1/2,j}(I_{m,i,j} - I_{m,i-1/2,j}) \tag{8}$$

$$I_{m,i,j+1/2} = I_{m,i,j} + f_{i,j-1/2}(I_{m,i,j} - - I_{m,i,j-1/2}) \tag{9}$$

These formulas change in the obvious way for rays traveling in the $-\mu$ and $-\xi$ directions. An alternative to diamond difference is the step approximation, in which the second term simply disappears, leaving $I_{m,i+1/2,j} = I_{m,i,j}$, etc.

If $\hat{n}\cdot\Omega_m < 0$, the $I^w_{m,i,j}$ term represents a source to the cell from emission and reflection at the boundary and we precompute these sources $S^w_{m,i,j}$ for all boundary cells before beginning the transport sweep for each ordinate direction. If $\hat{n}\cdot\Omega_m > 0$, this term is flux from the cell to the boundary and becomes part of the cell update. We use $I^w_{m,i,j} = I_{m,i,j}$ to compute these fluxes since the relation is already first order at the boundary.

Using the modified profile across the cell, the conservation relation becomes

$$\begin{aligned}&\frac{\mu_m}{\Delta x}[f_{i+1/2,j}(1 + f_{i-1/2,j})I_{m,i,j} - f_{i-1/2,j}(1 + f_{i+1/2,j})I_{m,i-1/2,j}]\\ &+ \frac{\xi_m}{\Delta y}[f_{i,j+1/2}(1 + f_{i,j-1/2})I_{m,i,j} - f_{i,j-1/2}(1 + f_{i,j+1/2})I_{m,i,j-1/2}]\\ &+ \left\lceil\frac{\hat{n}\cdot\Omega_m}{\Delta x\Delta y}L^w_{i,j}\right\rceil I_{m,i,j} + (\kappa+\sigma)F_{i,j}I_{m,i,j} = F_{i,j}S_{i,j} + S^w_{m,i,j}\end{aligned} \tag{10}$$

This expression is solved for $I_{m,i,j}$ and modified as before to limit the fluxes at the extrapolated faces. Note that since $I^w_{m,i,j}$ is not extrapolated, it does not have to be limited.

For each ordinate direction, after completing the transport sweep the reflection source is updated for all boundary cells with $\hat{n}\cdot\Omega_m > 0$. This update requires that we store intensities for all ordinate directions in the boundary cells, though we still do not have to store more than one direction at a time in the interior. (For the storage of boundary information we use a sparse data structure, which is essentially a list of mixed cells with pointers into the main grid.)

The general form of the boundary condition is

$$S^w_{m,i,j} = -\left\lfloor\frac{\hat{n}\cdot\Omega_m}{\Delta x\Delta y}L^w_{i,j}\right\rfloor \times \left\{\varepsilon I^w_b + \rho\frac{\sum_{\hat{n}\cdot\Omega_{m'}>0}(\hat{n}\cdot\Omega_{m'})w_{m'}L^w_{i,j}I^w_{m',i,j}}{\sum_{\hat{n}\cdot\Omega_{m'}>0}(\hat{n}\cdot\Omega_{m'})w_{m'}L^w_{i,j}}\right\} \tag{11}$$

To apply this in practice, we precompute the denominator of the reflection term and update the numerator after each ordinate sweep. If the ordinate set had the correct half-range first moment in the direction $\hat{n}$, the denominator would become simply $\pi L^w_{i,j}$ [cf. Eq. (5)], but it is not possible to choose an ordinate set for which $\sum_{\hat{n}\cdot\Omega_m>0}(\hat{n}\cdot\Omega_m)w_m = \pi$, for all possible $\hat{n}$.

The boundary condition (11) accounts for flux normal to the boundary in a conservative manner. It does not, however, correct for effects of the discrete ordinate representation in directions transverse to the boundary, which may not be quite symmetrical. An emitting wall with normal $\hat{n}$, for example, may produce radiation with a small bias toward some direction not parallel to $\hat{n}$. Chui and Raithby[12] discuss discrete ordinates in a control angle context, where this phenomenon takes the form of control angles straddling the boundary. Their algorithm splits the affected control angles in the boundary cells, treating incoming and outgoing portions separately. We have not attempted any similar correction in the present work. In a sense, while we have avoided stairstepping in the spatial discretization, we are still doing so in the angular discretization. Each ordinate direction is considered as directed either completely inward or completely outward on each boundary segment, never a mix of the two.

Cylindrical Coordinates

There are no new difficulties involved in taking this embedded boundary method to an axisymmetric coordinate system, the formulas just become more complicated. The fractions $F_{i,j}$ and $f_{i,j\pm1/2}$ are r weighted to be true volume and area fractions in three dimensions. That is, the volumes and areas are derived for the annular regions that result when cells are rotated about the central axis. The cell conservation relation with volume and area fractions takes the form

$$\begin{aligned}&\frac{\mu_{p,q}}{r_i\Delta r}(r_{i+1/2}f_{i+1/2,j}I_{p,q,i+1/2,j} - r_{i-1/2}f_{i-1/2,j}I_{p,q,i-1/2,j})\\ &+ \frac{\xi_p}{\Delta z}(f_{i,j+1/2}I_{p,q,i,j+1/2} - f_{i,j-1/2}I_{p,q,i,j-1/2})\\ &+ \frac{F_{i,j}}{r_iw_{p,q}}(\alpha_{p,q+1/2}I_{p,q+1/2,i,j} - \alpha_{p,q-1/2}I_{p,q-1/2,i,j})\\ &+ \frac{\hat{n}\cdot\Omega_{p,q}}{r_i\Delta r\Delta z}r^w_{i,j}L_{i,j}I^w_{p,q,i,j} + (\kappa+\sigma)F_{i,j}I_{p,q,i,j} = F_{i,j}S_{i,j}\end{aligned} \tag{12}$$

Uniform isotropic flow then yields an equation for the wall factor:

$$\begin{aligned}&\frac{\mu_{p,q}}{r_i\Delta r}(r_{i+1/2}f_{i+1/2,j} - r_{i-1/2}f_{i-1/2,j}) + \frac{\xi_p}{\Delta z}(f_{i,j+1/2} - f_{i,j-1/2})\\ &+ \frac{F_{i,j}}{r_iw_{p,q}}(\alpha_{p,q+1/2} - \alpha_{p,q-1/2}) + \frac{\hat{n}\cdot\Omega_{p,q}}{r_i\Delta r\Delta z}r^w_{i,j}L^w_{i,j} = 0\end{aligned} \tag{13}$$

To see that the weighting on the angular term is correct, consider replacing this term with a source function of the form $S = \mu/r$.

The spatial differences can use the same modified diamond difference as in Cartesian coordinates, while no modification is necessary in the angular term. Eliminating extrapolated values from the conservation relation then yields

$$\begin{aligned}&\frac{\mu_{p,q}}{r_i\Delta r}[r_{i+1/2}f_{i+1/2,j}(1 + f_{i-1/2,j})I_{p,q,i,j} - f_{i-1/2,j}(r_{i-1/2}\\ &+ r_{i+1/2}f_{i+1/2,j})I_{p,q,i-1/2,j}] + \frac{\xi_p}{\Delta z}[f_{i,j+1/2}(1 + f_{i,j-1/2})I_{p,q,i,j}\\ &- f_{i,j-1/2}(1 + f_{i,j+1/2})I_{p,q,i,j-1/2}] + \frac{F_{i,j}}{r_iw_{p,q}}[2\alpha_{p,q+1/2}I_{p,q,i,j}\\ &- (\alpha_{p,q+1/2} + \alpha_{p,q-1/2})I_{p,q-1/2,i,j}] + \left\lceil\frac{\hat{n}\cdot\Omega_{p,q}}{r_i\Delta r\Delta z}r^w_{i,j}L^w_{i,j}\right\rceil I_{p,q,i,j}\\ &+ (\kappa+\sigma)F_{i,j}I_{p,q,i,j} = F_{i,j}S_{i,j} + S^w_{p,q,i,j}\end{aligned} \tag{14}$$

which can be solved for $I_{p,q,i,j}$, and limited appropriately.

As in the preceding section, we update the boundary source term $S^w_{p,q,i,j}$ after every ordinate sweep so that the reflection source will always be up-to-date. The general form of the boundary condition follows the same pattern as for Cartesian coordinates.

Numerical Examples

The first two examples in this section establish second-order convergence of the heat transfer to the walls for straight and curved geometries, with black or gray walls. The final example shows a more complicated geometry representing an axisymmetric furnace. All ordinate values are taken from the S_6 set listed in Ref. 11, which has correct half-range first moments in the directions parallel to the coordinate axes.

Though we have written our code in a vectorizable form so that it will couple efficiently with fluid dynamics simulations running on Cray computers, all numerical examples presented here were computed on a DEC Alpha. Execution time scales with the number of points in the grid, with the largest grids (4096×4096) taking roughly 20 min per iteration. With black walls only one iteration is required, but with gray walls several iterations are needed to achieve convergence of the wall reflection source.

Black Circular Enclosure

We first consider the circular enclosure of unit diameter shown in Fig. 2. The walls are cold and black, and the interior is a uniform absorbing medium with blackbody emissive power $\pi I_b = 1$ and $\kappa = 2$. Table 1 gives the average heat transfer per unit length along the embedded boundary, which is the only boundary in the problem. Each r_i value given for convergence rate is a function of the three numbers a_{i-1}, a_i, a_{i+1} in the sequence to its left. We define

$$r_i = \log_2 \left| \frac{a_i - a_{i-1}}{a_{i+1} - a_i} \right| \tag{15}$$

so that r_i will indicate the order of accuracy of the scheme: 1 for first-order, 2 for second-order, etc.

We calculate the average flux through the boundary as follows:

$$\text{Flux} = \frac{1}{L} \sum_{i,j} (1 - \rho) \sum_{\hat{n} \cdot \Omega_m > 0} (\hat{n} \cdot \Omega_m) w_m L^w_{i,j} I^w_{m,i,j} \tag{16}$$

The L in this equation represents the total length of the circular boundary, but there is some question of how to best define this for the discrete problem at hand. For the first column of the table we use $L = \pi$, the length of the circle itself. For the second column we take L equal to the length of the polygonal representation of the circle on the discrete mesh. The errors are slightly greater for this case, but the convergence rate is more consistent. Finally, for the third column we take $L = 2A/r$, with $r = 0.5$ and A being the discrete area of the region. This gives the most consistent convergence rates, even for coarser grids, suggesting that this interpretation comes closest to capturing the discrete behavior of the system. (To see why scaling by area is reasonable, consider that since the algorithm is conservative, the heat transferred to the walls is equivalent to the difference between emission and absorption in the interior medium.)

All three columns are asymptotically equivalent because $L \to \pi$ and $A \to \pi/4$, both to second order. The overall convergence rate for the scheme appears to be a bit less than second order. In the next section we will see that a problem with straight sides comes much closer to second-order convergence. We speculate that the degraded performance for curved boundaries is an effect of the changing surface normals as the mesh is refined, interacting with the fixed ordinate directions, so that $\Sigma_{\hat{n} \cdot \Omega_m > 0} (\hat{n} \cdot \Omega_m) w_m$ takes on completely different values for each mesh.

For comparison, we ran the same problem using the method of Chai et al.[6] This approach uses a stairstep representation where the embedded boundary follows cell edges (Fig. 3). We create this representation for the circular enclosure by declaring cells more than half within the circle to be interior cells,

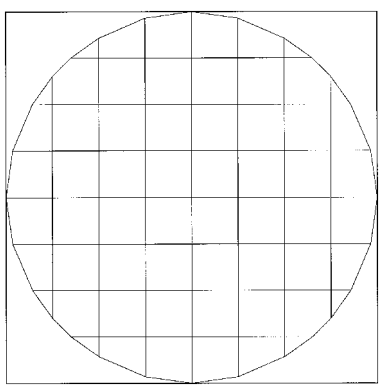

Fig. 2 Circular enclosure represented as an embedded boundary in a uniform grid: piecewise-linear boundary on an 8 × 8 grid.

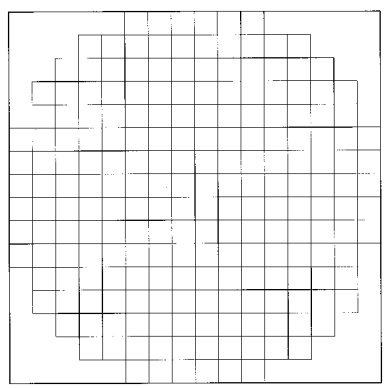

Fig. 3 Circular enclosure represented as an embedded boundary in a uniform grid: stairstep boundary on a 16 × 16 grid.

Table 1 Scaled heat transfer to the wall of a black circular enclosure of unit diameter[a]

Scaled by π			Scaled by length			Scaled by area		
Mesh	Absorption	Rate	Mesh	Absorption	Rate	Mesh	Absorption	Rate
8	0.8087779775	——	8	0.8148179684	——	8	0.8249516079	——
16	0.8152651038	2.363	16	0.8167151729	3.221	16	0.8193067597	1.681
32	0.8165258819	3.523	32	0.8169186113	0.110	32	0.8175457223	1.432
64	0.8166355411	1.185	64	0.8167301495	0.668	64	0.8168932723	1.437
128	0.8165873005	0.413	128	0.8166114962	1.125	128	0.8166522731	1.506
256	0.8165510810	1.178	256	0.8165571095	1.407	256	0.8165674273	1.587
512	0.8165350736	1.346	512	0.8165365979	1.463	512	0.8165391793	1.591
1024	0.8165287755	1.435	1024	0.8165291575	1.508	1024	0.8165298054	1.596
2048	0.8165264457	1.505	2048	0.8165265420	1.550	2048	0.8165267038	1.612
4096	0.8165256248	——	4096	0.8165256490	——	4096	0.8165256894	——

[a]Mesh sizes range from 8 × 8 to 4096 × 4096. Algorithm is diamond difference with volume and area fractions.

and the rest to be exterior cells. The boundary thus obtained corresponds to the domain boundary for a short distance along each side, but this does not cause any complications for the algorithm.

Table 2 shows the results using stair-stepping with diamond difference. The errors are larger than those computed using the volume and area fraction representation, and convergence is considerably more erratic. We do not show the total flux scaled by the length of the discrete boundary for this method because for all stairstep grids the length is exactly 4.

Though generally second-order, diamond difference calculations can be vulnerable to oscillations. We considered the possibility that the diamond difference scheme was interacting unfavorably with the stairstep boundary condition, and repeated the calculations using the step approximation. Table 3 shows the results, which are in fact somewhat worse than those found using diamond differences.

To complete our tests with this geometry, we also tried running the step approximation with the volume and area fraction representation of the boundary. The results in Table 4 show fairly smooth convergence, though at the end the sequence of approximations slightly overshoots the correct result and then turns back.

To summarize the results from these tests, all four combinations appear to be converging to the same value, which extrapolation in Table 1 gives as 0.816525. With either boundary condition the diamond difference scheme gives more accurate results than the step approximation. With either interior approximation the embedded boundary method of this paper gives both more consistent convergence rates and more accurate approximations to the converged solution.

The results in Tables 1–5 are presented to 10 decimal places for the purpose of showing the convergence behavior of the scheme. The numbers given are not in any sense correct to this level of accuracy, and so it is worthwhile to estimate the actual sizes of the errors in the calculation.

The largest error is that caused by the choice of ordinate discretization. The correct analytic value for this problem is 0.8143 (Ref. 13). The limiting value of 0.816525 seen in Table 1 shows the error in angular discretization with this particular S_6 ordinate set. The error is similar in size to those computed in Ref. 14 for three different ordinate sets, using a fixed un-

Table 2 Scaled heat transfer to the wall of a black circular enclosure of unit diameter[a]

Scaled by π			Scaled by area		
Mesh	Absorption	Rate	Mesh	Absorption	Rate
8	0.8407264938	——	8	0.8126831312	——
16	0.8379180881	−2.406	16	0.8099684030	−0.940
32	0.8230336450	1.884	32	0.8151760245	2.334
64	0.8190020066	1.697	64	0.8162087929	5.351
128	0.8177587720	0.076	128	0.8162341015	−4.005
256	0.8165792898	9.326	256	0.8166404370	2.391
512	0.8165811271	−2.856	512	0.8165629472	1.063
1024	0.8165678285	−0.588	1024	0.8165258542	7.882
2048	0.8165478419	0.068	2048	0.8165256969	−4.363
4096	0.8165287692	——	4096	0.8165289324	——

[a]Algorithm is diamond difference with stairstep boundary representation.

Table 3 Scaled heat transfer to the wall of a black circular enclosure of unit diameter[a]

Scaled by π			Scaled by area		
Mesh	Absorption	Rate	Mesh	Absorption	Rate
8	0.8270602567	——	8	0.7994727467	——
16	0.8342618825	−0.767	16	0.8064341543	−0.150
32	0.8220048459	2.311	32	0.8141570476	1.581
64	0.8195339913	0.952	64	0.8167389634	8.343
128	0.8182566087	0.066	128	0.8167310101	−5.527
256	0.8170364935	2.893	256	0.8170976750	0.590
512	0.8168722541	0.370	512	0.8168540678	0.691
1024	0.8167451848	0.409	1024	0.8167032013	0.991
2048	0.8166494629	0.582	2048	0.8166273152	0.866
4096	0.8165855293	——	4096	0.8165856925	——

[a]Algorithm is step approximation with stairstep boundary representation.

Table 4 Scaled heat transfer to the wall of a black circular enclosure of unit diameter[a]

Scaled by π			Scaled by length			Scaled by area		
Mesh	Absorption	Rate	Mesh	Absorption	Rate	Mesh	Absorption	Rate
8	0.7863290438	——	8	0.7922013850	——	8	0.8020537491	——
16	0.8044522767	1.308	16	0.8058831136	1.123	16	0.8084403283	0.555
32	0.8117730614	1.295	32	0.8121635049	1.225	32	0.8127869656	0.965
64	0.8147558764	1.370	64	0.8148502670	1.310	64	0.8150130144	1.210
128	0.8159100157	1.407	128	0.8159341914	1.377	128	0.8159749344	1.314
256	0.8163453849	1.541	256	0.8163514118	1.524	256	0.8163617271	1.493
512	0.8164950083	1.815	512	0.8164965326	1.810	512	0.8164991138	1.800
1024	0.8165375430	2.779	1024	0.8165379250	2.808	1024	0.8165385729	2.863
2048	0.8165437381	0.710	2048	0.8165438344	0.614	2048	0.8165439962	0.446
4096	0.8165399498	——	4096	0.8165399740	——	4096	0.8165400144	——

[a]Algorithm is step approximation with volume and area fractions.

structured grid roughly comparable to our 16 × 16 example. It is apparent from Table 1, that at this resolution, the errors caused by the spatial and angular discretizations are at about the same order of magnitude.

The ordinates and weights are tabulated in Ref. 11 to seven decimal places. We rescale these so that $\Sigma_m w_m$ is exactly 4π, and in the boundary condition (5) we replace π with the actual half-range first moment in the manner of Eq. (11). With these changes the system is conservative to machine precision for black walls. For gray walls, as in the next example, the system is conservative to the accuracy to which we solve the reflecting boundary condition, about 12 decimal places.

The errors caused by the spatial discretization are apparent from Table 1, being at about the seventh decimal place for the finest grids. Though the errors due to the choice of ordinate set are larger, they should not affect the observed convergence rates since the ordinate set is the same for all of the runs.

Gray Axisymmetric Enclosure

For our second example, we apply the embedded boundary method to the geometry shown in Fig. 4. The region is a unit square, except for the side on the right that slants inward at a 20-deg angle. We use axisymmetric coordinates with the left side falling on the axis, and so the actual three-dimensional geometry forms a frustum of a cone. Only the slanting wall is modeled as an embedded boundary, the axis and the two remaining walls fall on the edges of the domain and are modeled as in a uniform mesh. Note that two cells contain both domain and embedded boundaries.

The interior is a uniform absorbing medium with blackbody emissive power $\pi I_b = 1$ and $\kappa = 2$. The walls are all gray with $\rho = \varepsilon = 0.5$ and $\pi I_b = 0.5$. The radiative transport equation (RTE) is solved by initializing the wall reflection sources to zero and iterating until the change in reflection source from one iteration to the next is reduced by a factor of 10^{-12}. For the present problem, with immediate updates at each boundary, we saw approximately one order of magnitude reduction per iteration.

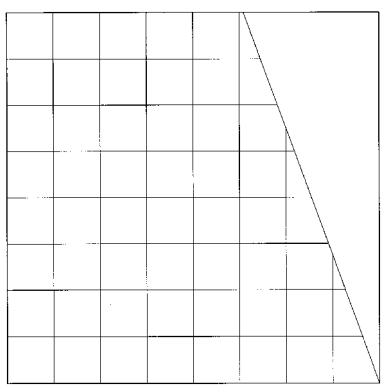

Fig. 4 Axisymmetric enclosure represented using a combination of embedded and domain boundaries.

Table 5 gives the average heat transfer per unit area along the boundaries. The first column shows absorption alone along the slanting wall, the second column shows absorption minus emission, while the third column shows this same quantity for all three walls combined. Because the walls are all straight, the surface areas and enclosed volume are always correct to machine precision. Since L is a constant, the scaling issues of the previous example do not arise. The convergence rate is nearly 2, and is roughly the same for each column. Thus, the method is second-order for straight sides, and performs correctly with emitting and reflecting walls and with interactions between domain and embedded boundaries.

We do not present results from the stair-stepping boundary condition and/or the step approximation with this geometry, as they roughly repeat the trends shown for the circular geometry.

Axisymmetric Furnace

For our final example, we plot contours of incident energy $G_{i,j} = \Sigma_{p,q} w_{p,q} I_{p,q,i,j}$ for the furnace geometry shown in Figs. 5 and 6. Furnace dimensions, wall temperatures, emissivities, and reflectivities are taken from Ref. 15, while the interior is taken to be a cold absorbing medium with $\kappa = 0.2\ \mathrm{m}^{-1}$. A 40 × 227 grid is used with axisymmetric coordinates. Ray effects are visible at the lower left because of the relatively cold inlet region, and in the exhaust duct because of the temperature differential between the duct and the furnace.

This example is provided to show the use of the embedded boundary algorithm on a more complex geometry. It is not a

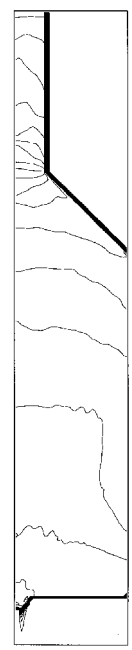

Fig. 5 Contours of incident energy in the BERL geometry.

Table 5 Scaled heat transfer to the wall of an axisymmetric gray radiating enclosure

Embedded wall absorption			Embedded wall net flux			Total wall net flux		
Mesh	Absorption	Rate	Mesh	Absorption	Rate	Mesh	Absorption	Rate
8	0.4603048202	——	8	0.2102362789	——	8	0.2085897529	——
16	0.4605075961	2.598	16	0.2101239715	0.005	16	0.2084476802	0.715
32	0.4604741120	−0.332	32	0.2100120832	0.864	32	0.2083611186	1.132
64	0.4604319634	0.935	64	0.2099505878	1.198	64	0.2083216156	1.322
128	0.4604099129	1.444	128	0.2099237879	1.527	128	0.2083058114	1.555
256	0.4604018086	1.697	256	0.2099144862	1.733	256	0.2083004335	1.752
512	0.4603993098	1.839	512	0.2099116890	1.855	512	0.2082988363	1.871
1024	0.4603986113	1.933	1024	0.2099109159	1.939	1024	0.2082983996	1.931
2048	0.4603984284	1.944	2048	0.2099107143	1.949	2048	0.2082982850	1.963
4096	0.4603983809	——	4096	0.2099106621	——	4096	0.2082982556	——

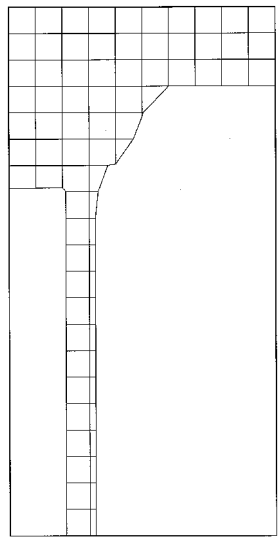

Fig. 6 Detail of grid around inlet and burner region at lower left.

realistic model of radiation in the furnace since fluid emission is neglected; see Ref. 5 for a more complete simulation.

The geometry includes fine details of the burner region that are not well-represented on the discrete mesh. The inset shows how the grid in this region only roughly captures the shape of the burner.[15] Accurate simulations will require a combination of the embedded boundary techniques presented here, with the adaptive mesh refinement algorithms presented in Refs. 3 and 16.

Conclusions

We have presented an extension of the discrete ordinates method for radiative transfer calculations to domains with embedded boundaries. An embedded boundary is represented as a piecewise-linear tracked front within a regular mesh using volume and area fractions for each cell. The method supports both Cartesian and axisymmetric meshes. Both embedded and domain-wall boundary conditions can coexist within a single problem or even within a single cell.

The discretization is equivalent to second-order diamond differences in the mesh interior, and reduces to first-order at the boundaries. Flux limiting is implemented in a way that does not inhibit vectorization. The solution strategy is based on transport sweeps, iterated to convergence of the wall reflection and scattering terms. Because of the form of the reflection updates, energy is conserved to the level of the convergence tolerance. (With minor modifications the method could conserve to machine precision independent of this tolerance, but at the expense of slower convergence.)

Numerical examples illustrate the method for a curved embedded boundary in Cartesian coordinates, and for a combination of straight embedded and domain-wall boundaries in axisymmetric coordinates. Both black and gray walls are considered. The results show clear second-order convergence of the heat transfer to the walls for the straight wall example. The curved example shows a convergence rate intermediate between first and second order. A final example shows the method applied to a more complex geometry, that of an axisymmetric furnace.

Acknowledgments

This work was supported by the Applied Mathematical Sciences Program and the HPCC Grand Challenge Program of the Office of Mathematics, Information and Computational Sciences of the U.S. Department of Energy, Contract DE-AC03-76SF00098.

References

[1]Purvis, J. W., and Burkhalter, J. E., "Prediction of Critical Mach Number for Store Configurations," *AIAA Journal*, Vol. 17, No. 11, 1979, pp. 1170–1177.

[2]Berger, M. J., and LeVeque, R. J., "An Adaptive Cartesian Mesh Algorithm for the Euler Equations in Arbitrary Geometries," *AIAA 9th Computational Fluid Dynamics Conf.* (Buffalo, NY), AIAA, Washington, DC, 1989, pp. 1–7.

[3]Pember, R. B., Bell, J. B., Colella, P., Crutchfield, W. Y., and Welcome, M. L., "An Adaptive Cartesian Grid Method for Unsteady Compressible Flow in Irregular Regions," *Journal of Computational Physics*, Vol. 120, No. 2, 1995, pp. 278–304.

[4]Almgren, A. S., Bell, J. B., Colella, P., and Marthaler, T., "A Cartesian Grid Projection Method for the Incompressible Euler Equations in Complex Geometries," *SIAM Journal on Scientific Computing* (to be published).

[5]Pember, R. B., Almgren, A. S., Crutchfield, W. Y., Howell, L. H., Bell, J.. B., Colella, P., and Beckner, V. E., "An Embedded Boundary Method for the Modeling of Unsteady Combustion in an Industrial Gas-Fired Furnance," *Proceedings of the 1995 Fall Meeting of the Western States Section of the Combustion Institute* (Stanford, CA), The Combustion Inst., Pittsburgh, PA, 1995.

[6]Chai, J. C., Lee, H. S., and Patankar, S. V., "Treatment of Irregular Geometries Using a Cartesian Coordinates Finite-Volume Radiation Heat Transfer Procedure," *Numerical Heat Transfer*, Vol. 26, Pt. B, 1994, pp. 225–235.

[7]Carlson, B. G., and Lathrop, K. D., "Transport Theory — The Method of Discrete Ordinates," *Computing Methods in Reactor Physics*, edited by H. Greenspan, C. N. Kelber, and D. Okrent, Gordon and Breach, New York, 1968, pp. 171–266.

[8]Lewis, E. E., and Miller, W. F., Jr., *Computational Methods of Neutron Transport*, American Nuclear Society, La Grange Park, IL, 1993.

[9]Fiveland, W. A., "Discrete-Ordinates Solutions of the Radiative Transport Equation for Rectangular Enclosures," *Journal of Heat Transfer*, Vol. 106, No. 4, 1984, pp. 699–706.

[10]Lathrop, K. D., and Carlson, B. G., "Discrete Ordinates Angular Quadrature of the Neutron Transport Equation," Los Alamos Scientific Lab., 3186, Los Alamos, CA, 1965.

[11]Fiveland, W. A., "Three-Dimensional Radiative Heat-Transfer Solutions by the Discrete-Ordinates Method," *Journal of Thermophysics and Heat Transfer*, Vol. 2, No. 4, 1988, pp. 309–316.

[12]Chui, E. H., and Raithby, G. D., "Computation of Radiant Heat Transfer on a Nonorthogonal Mesh Using the Finite-Volume Method," *Numerical Heat Transfer*, Vol. 23, Pt. B, 1993, pp. 269–288.

[13]Modest, M. F., *Radiative Heat Transfer*, McGraw–Hill, New York, 1993, pp. 472–475.

[14]Fiveland, W. A., and Jessee, J. P., "Comparison of Discrete Ordinates Formulations for Radiative Heat Transfer in Multidimensional Geometries," *Journal of Thermophysics and Heat Transfer*, Vol. 9, No. 1, 1995, pp. 47–54.

[15]Kaufman, K. C., Fiveland, W. A., Peters, A. A. F., and Weber, R., "The BERL 300kW Unstaged Natural Gas Flames with a Swirl-Stabilized Burner, Case 1: Hot-Wall Conditions," Gas Research Inst., Contract 5093-260-2729, Nov. 1994.

[16]Jessee, J. P., Fiveland, W. A., Howell, L. H., Colella, P., and Pember, R. B., "An Adaptive Mesh Refinement Algorithm for the Discrete Ordinates Method," *Proceedings of the 1996 National Heat Transfer Conference* (Houston, TX), 1996.